JOURNAL OF THE ROYAL SOCIETY Interface

J. R. Soc. Interface (2011) **8**, 1594–1603
doi:10.1098/rsif.2011.0108
Published online 20 April 2011

Effect of reverse flow on the pattern of wall shear stress near arterial branches

A. Kazakidi[1,2], A. M. Plata[1], S. J. Sherwin[1,*] and P. D. Weinberg[2]

[1]*Department of Aeronautics, and* [2]*Department of Bioengineering, Imperial College London, London SW7 2AZ, UK*

Atherosclerotic lesions have a patchy distribution within arteries that suggests a controlling influence of haemodynamic stresses on their development. The distribution near aortic branches varies with age and species, perhaps reflecting differences in these stresses. Our previous work, which assumed steady flow, revealed a dependence of wall shear stress (WSS) patterns on Reynolds number and side-branch flow rate. Here, we examine effects of pulsatile flow. Flow and WSS patterns were computed by applying high-order unstructured spectral/hp element methods to the Newtonian incompressible Navier–Stokes equations in a geometrically simplified model of an aorto-intercostal junction. The effect of pulsatile but non-reversing side-branch flow was small; the aortic WSS pattern resembled that obtained under steady flow conditions, with high WSS upstream and downstream of the branch. When flow in the side branch or in the aortic near-wall region reversed during part of the cycle, significantly different instantaneous patterns were generated, with low WSS appearing upstream and downstream. Time-averaged WSS was similar to the steady flow case, reflecting the short duration of these events, but patterns of the oscillatory shear index for reversing aortic near-wall flow were profoundly altered. Effects of reverse flow may help explain the different distributions of lesions.

Keywords: haemodynamics; atherosclerosis; wall shear stress; arterial branches; reverse flow; oscillatory shear index

1. INTRODUCTION

Atherosclerosis is a disease of large systemic arteries. Its early lesions (fatty streaks) are characterized by the focal accumulation of lipids, fibrous proteins and inflammatory cells within the arterial intima. A striking feature of the disease is the characteristic distribution of these lesions, particularly in areas of curvature and branching. Wall shear stress (WSS), among other haemodynamic factors, may play a significant role in the development of the disease and account for this localization; lesions are currently thought to develop in regions where WSS is low on average and fluctuates during the cardiac cycle [1,2].

The location of fatty streaks in human arteries varies with age; other species, such as apolipoprotein E knockout (ApoE−/−) mice and cholesterol-fed rabbits, show some but not all of the human patterns [3]. Variation in lesion patterns between species and/or with age may reflect differences in the distribution of WSS. In a previous investigation [4], we showed that the pattern of WSS around arterial side branches was dependent on Reynolds number and flow partition, both of which may vary between species and between ages within a species. Here, we investigate effect of reverse flow on these patterns. High-order spectral/hp element methods [5] were used to examine cases of reversing and non-reversing flow within an idealized geometry representing one intercostal artery branching perpendicularly from the thoracic aorta.

*Author for correspondence (s.sherwin@imperial.ac.uk).

2. METHODS

2.1. Geometry

Paired intercostal arteries originate from the dorsal wall of the descending thoracic aorta in humans, rabbits and mice. Although there are variations in their geometry [6], the junction may usefully be described in computational investigations by a simplified model in which the thoracic aorta is represented as a rectangular channel and the intercostal artery as a cylinder emerging perpendicularly from it (figure 1). The assumption of a flat aortic wall around the junction is justified by the large difference between the diameters of the intercostal artery and the thoracic aorta. We have demonstrated previously [4] that more complex geometrical features (such as surface curvature and pairing of branches) have qualitatively little influence on the pattern of aortic WSS near intercostal ostia.

In the geometry shown in figure 1, the ratio of the branch diameter (D) to the width (D_a) of the rectangular channel, equivalent to the aortic diameter, was assumed to be 0.1 [7–12]. In addition to this width of $10D$ in the crossflow (y) direction, the rectangular channel had length $26D$ and height $5D$ in the axial (x) and perpendicular (z) directions, respectively; thus only

Received 25 February 2011
Accepted 29 March 2011

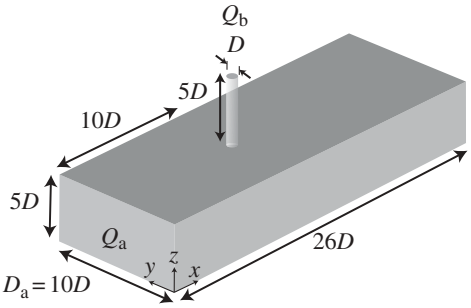

Figure 1. Computational domain representing an intercostal artery emerging perpendicularly from the thoracic aorta. The unit of length, D, is the diameter of the intercostal artery. Q_a and Q_b indicate the flow rates in the aorta and the side branch, respectively.

the half-height of the aortic lumen was included. (The coordinate origin is also displayed in figure 1.) The cylindrical tube representing the intercostal artery had length $5D$ and its upstream lip was placed along the longitudinal centreline of the aortic wall, at a distance $10D$ from the upstream end of the aortic section. Q_a (figure 1) is the aortic flow rate and Q_b is the side-branch pipe flow rate.

2.2. Governing equations

The incompressible Navier–Stokes equations and Newtonian rheology were used to describe the flow through the aorto-intercostal junction

$$\rho\frac{\partial \mathbf{u}}{\partial t} + \rho(\mathbf{u}\cdot\nabla)\mathbf{u} = -\nabla p + \mu\nabla^2\mathbf{u}$$

and

$$\nabla\cdot\mathbf{u} = 0,$$

where $\mathbf{u} = [u,v,w]$ is the velocity vector, ρ is the fluid density, p is the static pressure and μ is the dynamic viscosity. Flow is characterized by a mean Reynolds number defined as $Re_m = \rho\bar{u}_a D_a/\mu$, where $\bar{u}_a$ is the temporally and cross-sectionally averaged velocity of the fluid in the aorta. Another parameter is required in order to describe fully the unsteady/pulsatile flow. Here, we use the reduced velocity parameter U_{red}, which is the reciprocal of the Strouhal number, St, and is defined [13] as

$$U_{red} = \frac{UT}{D_i},$$

where U is a velocity scale (e.g. the time and sectionally averaged velocity in the aorta), T is the pulse duration and D_i is a representative length scale such as the aortic or branch diameter. U_{red} can be seen as the length, expressed in diameters, that the average fluid travels in one period T. It is related to the Womersley number α ($\alpha = (D_i/2)\sqrt{\omega\rho/\mu}$) and the mean Reynolds number Re_m (based on time and sectionally averaged aortic velocity) according to $U_{red} = \pi Re_m/2\alpha^2$; where ω is the angular frequency ($\omega = 2\pi/T$).

Flow at the entrance of the aortic segment was considered two-dimensional (channel flow) in the xz-plane.

WSS patterns were computed for four combinations of conditions specified at the aortic inflow and the side-branch outflow: (i) steady aortic and side-branch flow; (ii) steady aortic flow with pulsatile but non-reversing side-branch flow, the latter consisting of a steady component plus a smaller oscillatory (sinusoidal) component with a mean of zero; (iii) steady aortic flow with pulsatile reversing side-branch flow (comprising a steady component and a larger oscillatory component); and (iv) pulsatile aortic flow that reversed near the wall but not at the centreline, with pulsatile non-reversing side-branch flow.

For steady flow, a parabolic inlet velocity profile was imposed, which in non-dimensional form can be written as

$$\frac{u_a}{\bar{u}_a}(z) = \frac{3}{2}\left(1 - \frac{z^2}{25D^2}\right).$$

Since, for the range of velocities studied, aortic flow is undisturbed far from the branch [4], the peak of the parabolic velocity profile was imposed at the bottom plane of the domain (opposite to the aortic wall) and the same velocity profile as at the inflow was imposed along the length of the lateral planes of the domain. The aortic flow rate was defined as $Q_a = \bar{u}_a 100D^2$, where $100D^2$ is the inflow area of a channel having double the height of that shown in figure 1. The no-slip condition was applied on the aortic and side-branch walls.

Under the influence of a periodic pressure gradient, the velocity for channel flow can be written in a complex form [14,15] as

$$u_{osc}(z,t) = \frac{A_p}{i\omega\rho}\left[1 - \frac{\cosh(\alpha i^{1/2} z/5D)}{\cosh(\alpha i^{1/2})}\right]e^{i\omega t},$$

where $i = (-1)^{1/2}$, A_p is the amplitude of the periodic pressure gradient ($\partial p/\partial x = -A_p e^{i\omega t}$) with a zero average, and $5D$ is the channel half-height. The expression for the real part of the above equation can be found in Loudon & Tordesillas [15]. To obtain pulsatile aortic flow, the temporal waveform of the sectionally averaged aortic inflow was described by a steady component plus a single sinusoidal harmonic. This procedure is valid owing to the linearity of the fully developed Navier–Stokes equations. The aortic inflow velocity, $u_a = u_a(z,t)$, can be written in non-dimensional form (with $z = 0$ being the channel centreline) as

$$\frac{u_a}{\bar{u}_a}(z,t) = \frac{3}{2}\left(1 - \frac{z^2}{25D^2}\right) + \frac{3\omega\rho}{A_p a^2}\Re\{u_{osc}(z,t)\},$$

where $\Re\{\ \}$ denotes the real part of the complex function. The above equation was imposed on the bottom plane of the computational domain as well as at the inflow. The unsteady component, which has a zero temporal average, can also be expressed as

$$\bar{u}_{osc}(t) = \frac{A_p}{i\omega\rho}\left[1 - \frac{1}{\alpha i^{1/2}}\tanh(\alpha i^{1/2})\right]e^{i\omega t},$$

when averaged over the full-height, cross-sectional inflow area, $100D^2$.

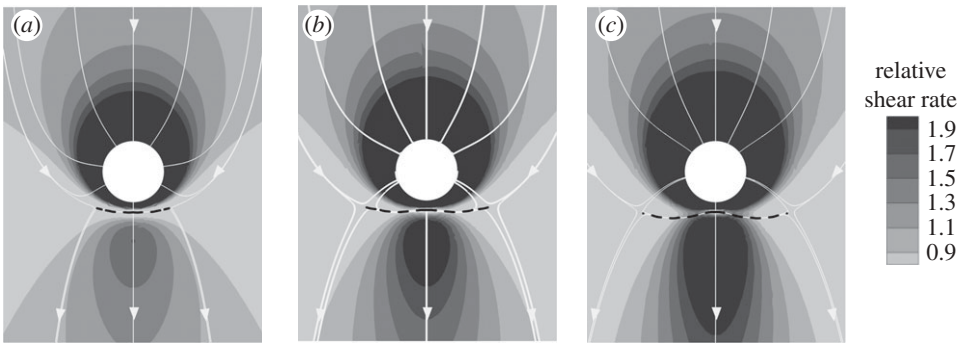

Figure 2. Magnitude and direction of non-dimensionalized aortic WSS around the ostium of an idealized intercostal artery for steady aortic flow with Reynolds numbers of (*a*) 250, (*b*) 500 and (*c*) 750, and steady intercostal flow (fully developed pipe flow at the outlet, $Q_b : Q_a = 0.79\%$). A subregion of the computational domain approximately $5.5D$ long $\times$ $4.3D$ wide is shown. Mean aortic flow is from top to bottom. White lines are surface streamlines and arrows indicate the direction of WSS along them. Dashed lines indicate flow stagnation.

Fully developed periodic pipe flow was imposed at the outflow of the side branch. This is described, according to Womersley [16], by the real part of the following expression:

$$w(r,t) = \frac{A'_p}{i\omega\rho}\left\{1 - \frac{J_o[\alpha i^{3/2} 2(r - D/2)/D]}{J_o(\alpha i^{3/2})}\right\} e^{i\omega t},$$

where r is the radial distance from the centreline of the cylindrical branch (radius $= D/2$), J_o ($xi^{3/2}$) is a complex Bessel function, and A'_p is the amplitude of the driving pressure gradient ($\partial p/\partial z = -A'_p e^{i\omega t}$).

The time-averaged WSS magnitude was calculated as

$$\tau_{av} = \frac{1}{T}\int_0^T |\mathbf{t}_w| dt,$$

where $\mathbf{t}_w$ is the instantaneous WSS vector and $|\mathbf{t}_w|$ is its magnitude.

The oscillatory shear index (OSI) was defined [17] as

$$OSI = \frac{1}{2}\left(1 - \frac{|1/T\int_0^T \mathbf{t}_w dt|}{1/T\int_0^T |\mathbf{t}_w| dt}\right).$$

For flow aligned to the vessel centreline this index is a measure of the fraction of one period during which the sign of the WSS is reversed. It takes values in the range of 0 to 0.5, with 0 corresponding to unidirectional flow, and 0.5 to purely oscillatory flow.

All results were computed for a cycle-averaged flow partition, $Q_b : Q_{am}$, of 0.79 per cent (the ratio for which WSS was most extensively characterized in Kazakidi *et al.* [4]), where Q_{am} is the cycle-averaged aortic flow rate.

2.3. Computational methods

A hybrid mesh of body-conforming prismatic and unstructured tetrahedral elements was created using non-proprietary software [18,19]. The prismatic boundary layer mesh generated at the walls had thickness $0.3D$. The mesh contained 452 prismatic and 2116 tetrahedral elements. To test numerical accuracy, a mesh with 908 prismatic and 6536 tetrahedral elements was also created. The increase in mesh elements produced an approximately 0.01 per cent change in the streamwise force on the aortic wall.

A validated spectral/hp element method was used to compute the flow solution [20–22]. The order of the polynomial expansion within each element was six, corresponding to 266 336 local degrees of freedom per variable. An increase in order from four to six reduced the streamwise force over the whole domain by approximately 2 per cent.

3. RESULTS

The magnitude of instantaneous aortic WSS around the ostium of the intercostal artery, normalized by the instantaneous inflow WSS, is shown in figures 2–5 for the four combinations of aortic inflow and side-branch outflow described above. The patterns are overlaid by streamlines indicating flow direction immediately above the wall.

3.1. Steady flow

Figure 2*a–c* shows patterns of WSS for steady aortic flow at $Re = 250$, 500 and 750. These values are equivalent to the minimum, mean and maximum, respectively, for pulsatile flow with a mean of 500 and a peak-to-mean ratio of 1.5 for the aortic inflow velocity averaged over the cross section (i.e. the case considered below). Steady, fully developed pipe flow was imposed at the outflow of the side branch. Increasing the Reynolds number reduced WSS at the sides and increased it upstream and downstream of the ostium. Surface streamlines converged towards the ostium in the area upstream of the branch (suggesting local acceleration of fluid particles) and diverged in the area downstream (suggesting local deceleration). The streamlines were symmetrical about the centreline, although this was not explicitly imposed (see [4] for an analysis of the flow features underlying similar patterns).

3.2. Non-reversing pulsatile side-branch flow

Figure 3 displays instantaneous WSS patterns for steady aortic flow ($Re = 500$) and non-reversing pulsatile flow in the side branch. U_{redb}, defined according to the side-branch diameter and mean sectionally averaged aortic velocity, was 40 (equivalent to $St = 0.025$ at the branch

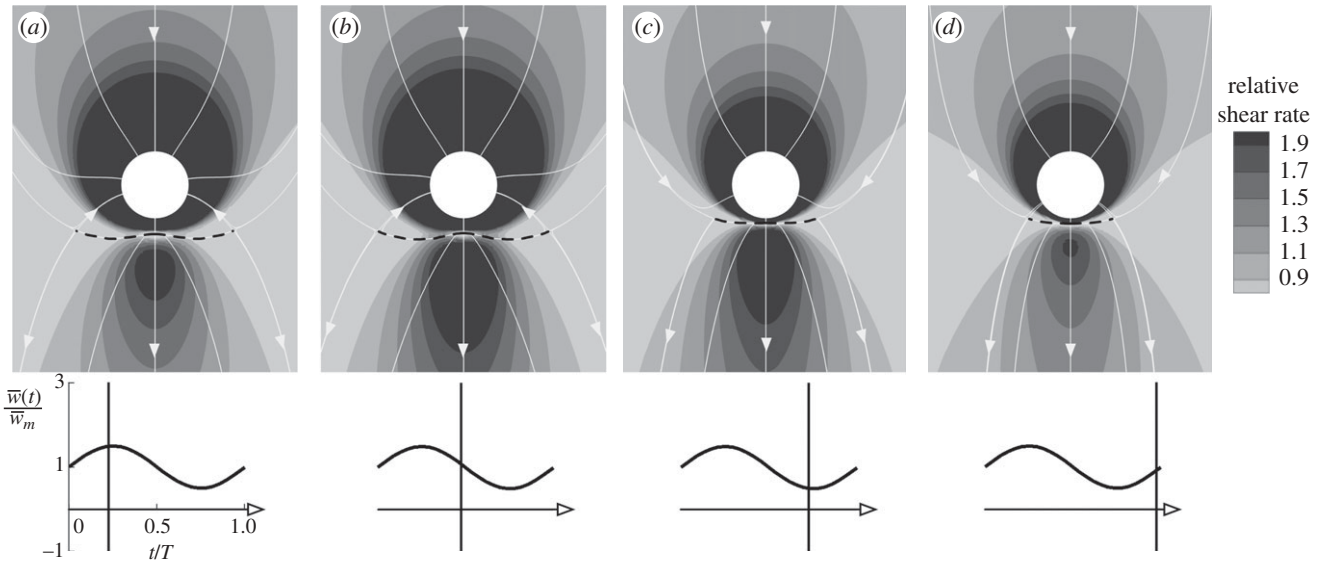

Figure 3. Magnitude and direction of non-dimensionalized instantaneous aortic WSS for steady aortic flow of $Re = 500$ and non-reversing pulsatile flow in the side branch ($Q_b : Q_a = 0.79\%$). Time points depicted: $t/T =$ (*a*) 0.225, (*b*) 0.475, (*c*) 0.725, and (*d*) 0.975. (Flow velocity in the side branch, averaged across its cross section and scaled by the time-averaged value, is plotted under the maps, with a vertical line indicating the part of the cycle corresponding to each time point; peak flow is at $t/T = 0.25$.) A subregion of the computational domain approximately $5.5D$ long $\times$ $4.3D$ wide is shown. Mean aortic flow is from top to bottom. Dashed lines indicate flow stagnation. ($U_{redb} = 40$; side branch peak-to-mean flow ratio = 1.5.)

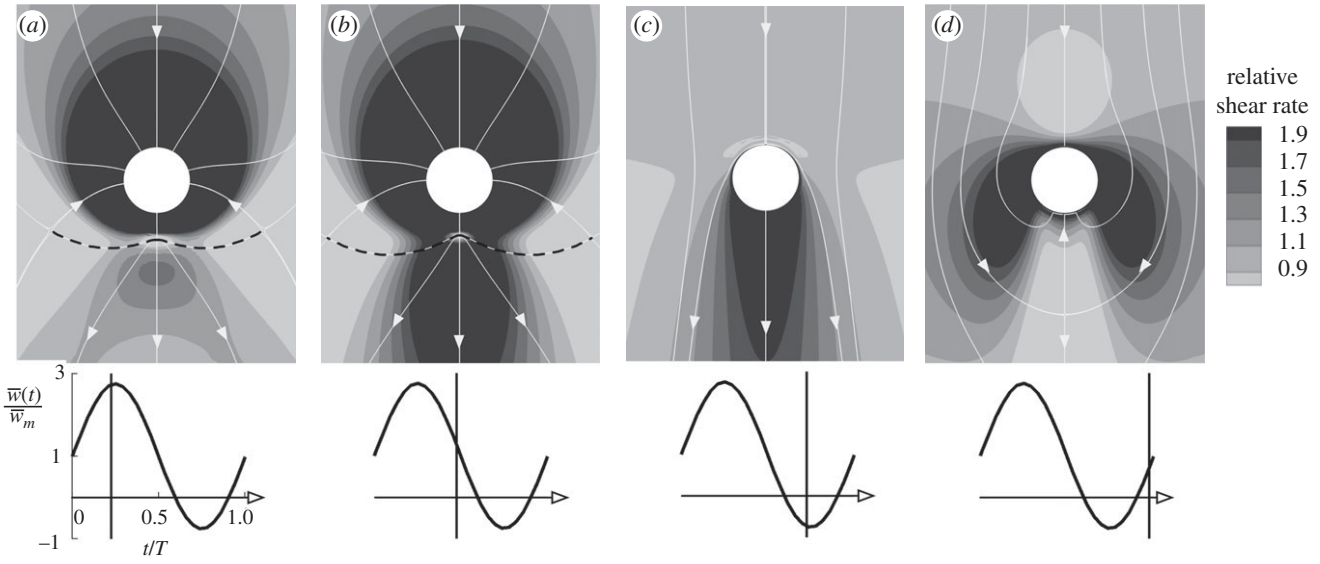

Figure 4. Magnitude and direction of non-dimensionalized instantaneous aortic WSS for a steady aortic flow of $Re = 500$ and reversing flow in the side branch ($Q_b : Q_a = 0.79\%$). Time points shown: $t/T =$ (*a*) 0.225, (*b*) 0.475, (*c*) 0.725, and (*d*) 0.975. (Flow velocity in the side branch, averaged across its cross section and scaled by the time-averaged value, is plotted under the maps, with a vertical line indicating the part of the cycle corresponding to each time point; peak flow is at $t/T = 0.25$.) A subregion of the computational domain approximately $5.5D$ long $\times$ $4.3D$ wide is shown. Mean aortic flow is from top to bottom. Dashed lines indicate flow stagnation. ($U_{redb} = 40$; side-branch peak-to-mean flow ratio = 2.75.)

outflow) and the side-branch peak-to-mean flow ratio was 1.5. The figure shows four discrete time points during the cycle: $t/T = 0.225; 0.475; 0.725$ and 0.975. (Peak flow is at $t/T = 0.25$.) Regions of high WSS around the ostial lip, as well as upstream and downstream of it, and of low WSS lateral to it, were largest during the deceleration phase of the cycle (figure 3*b*), and smallest during acceleration (figure 3*d*). Intermediate patterns were obtained at the other time points (figure 3*a*,*c*). However, changes in WSS pattern over the cycle were small; the main features remained qualitatively similar to the steady flow case for the equivalent mean Re and flow partition $Q_b : Q_{am}$ (figure 2*b*). In all cases, surface streamlines converged towards the branch in the upstream region and diverged in the downstream region.

3.3. Reversing side-branch flow

The peak-to-mean flow ratio in the side branch was increased to 2.75, making the flow reverse for approximately one-third of the cycle. Instantaneous WSS patterns, again at $t/T = 0.225; 0.475; 0.725$ and 0.975,

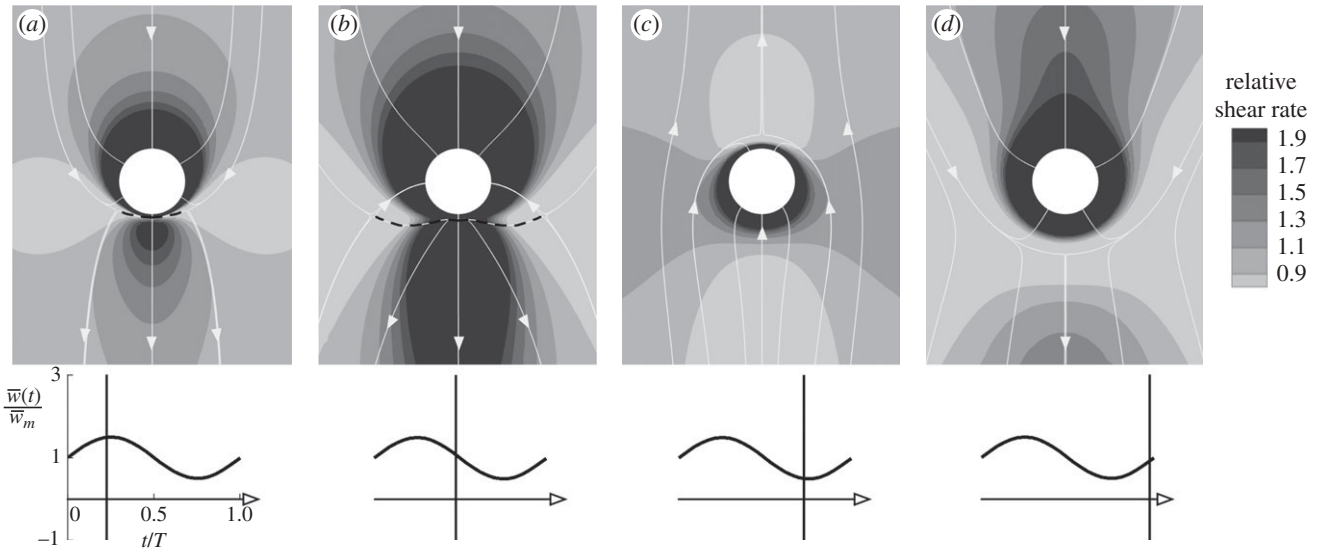

Figure 5. Magnitude and direction of non-dimensionalized instantaneous aortic WSS for a pulsatile channel-flow solution in the aorta ($Re_m = 500$) and non-reversing flow in the side branch ($Q_b : Q_{am} = 0.79\%$, where Q_{am} is the cycle-averaged aortic flow rate). Time points shown: t/T= (*a*) 0.225, (*b*) 0.475, (*c*) 0.725 and (*d*) 0.975. (Flow velocity in the side branch, averaged across its cross section and scaled by the time-averaged value, is plotted under the maps, with a vertical line indicating the part of the cycle corresponding to each time point; peak flow is at $t/T = 0.25$.) A subregion of the computational domain approximately $5.5D$ long $\times$ $4.3D$ wide is shown. U_{red} was four ($\alpha = 14$) and the aortic peak-to-mean flow ratio was 1.5. Side-branch peak-to-mean flow ratio = 1.5 ($U_{redb} = 40$).

are shown in figure 4. Initiation of side-branch flow reversal towards the end of the deceleration phase (figure 4*c*) resulted in a WSS pattern that differed substantially from the steady flow case (figure 2*b*). A confined, almost triangular, region of high shear was located immediately downstream of the ostium, WSS values on the ostial lip were elevated, and a small region of low WSS appeared slightly upstream of the upstream margin. Laterally, regions of low WSS were located approximately one branch diameter lateral to the ostium. Surface streamlines slightly converged in the upstream and lateral regions and diverged downstream of the branch. During acceleration (figure 4*d*), the region of low WSS values upstream of the branch orifice increased in size and moved further upstream, while the triangular region of high shear downstream of the ostium was replaced with a streak of low shear values. The high WSS values surrounding the lip were shifted and extended laterally and further downstream. Surface streamlines diverged in the upstream and lateral regions, and converged in the downstream region. Near the middle of the deceleration phase (figure 4*b*), the pattern of WSS resembled that observed under steady flow conditions—high shear values around the branch, as well as upstream and downstream, and low values laterally—although these features were enlarged. The pattern obtained in late acceleration (figure 4*a*) was intermediate; it showed the steady flow characteristics in the upstream area, but in the downstream area low shear values were replaced with higher shear values.

3.4. Non-reversing pulsatile side-branch flow and reversing aortic near-wall flow

U_{red}, defined according to the diameter and mean velocity at the aortic inlet, was four (equivalent to $St = 0.25$ or $\alpha = 14$) and the peak-to-mean inflow ratio was 1.5. The bulk of the flow was non-reversing but reversal did occur close to the wall during part of the cycle. At the side branch, U_{redb} was kept equal to 40 ($St = 0.025$) and the peak-to-mean flow ratio was returned to 1.5 (non-reversing). The Womersley-type velocity waveform at the branch outflow had the same frequency and was in phase with the velocity at the aortic inflow. Figure 5 displays instantaneous WSS patterns at the four points in the cycle described above. Regions of high WSS were most extensive near the middle of the deceleration phase (figure 5*b*). Reversal of the near-wall fluid in the aorta in late deceleration produced a different pattern (figure 5*c*), in which WSS was lowest in regions upstream and downstream of the ostium, and high WSS was restricted to a small region in the vicinity of the ostial lip and lateral to the ostium. Just after the near-wall aortic flow became forward-moving again, near the middle of the acceleration phase (figure 5*d*), a broad region of high WSS encircled the ostium; it extended approximately $0.4D$ to the sides, $0.35D$ downstream and $0.8D$ upstream of it. Low shear values were observed in a wide region downstream and lateral to the ostium. The pattern gradually returned to the steady flow characteristics of high values upstream and downstream of the branch, and low values at the sides, late in the acceleration phase (figure 5*a*). During most of the cycle, the surface streamlines converged towards the branch upstream and diverged downstream. However, during reversal of the aortic near-wall fluid at the end of the deceleration phase, the streamline pattern was reversed (figure 5*c*): streamlines converged towards the branch but from the opposite direction. Stagnation lines were observed downstream of the ostium in late acceleration and near mid-deceleration but were absent in late deceleration/early acceleration.

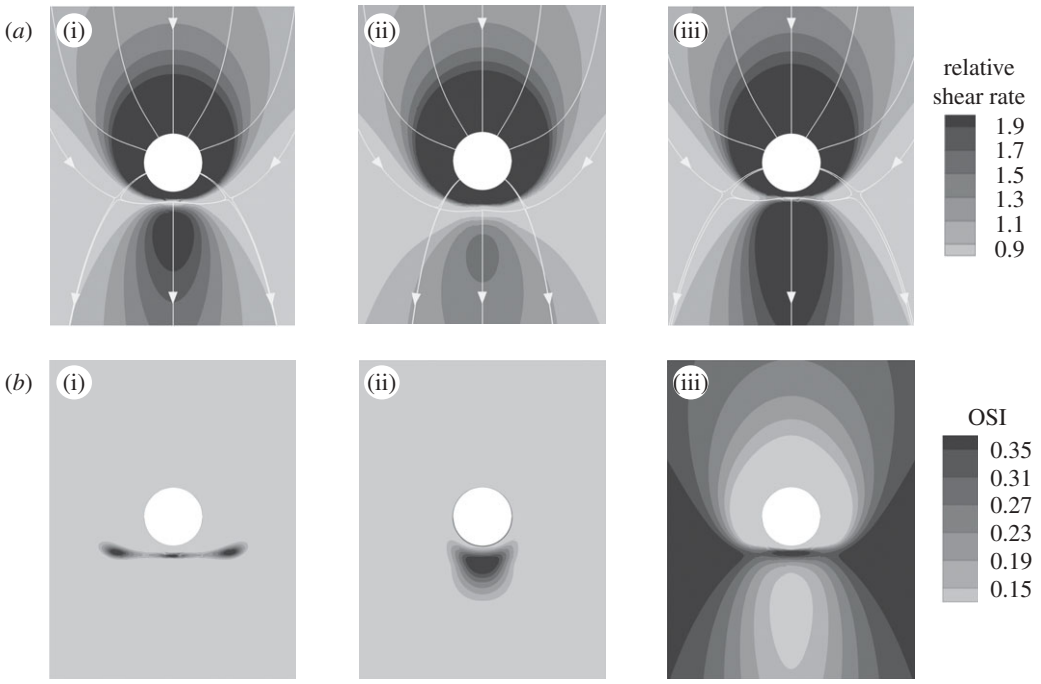

Figure 6. Time-averaged WSS (*a* (i–iii)) and OSI (*b* (i–iii)) patterns for the cases presented in figures 3–5, respectively.

3.5. Time-averaged wall shear stress

Time-averaged WSS patterns for the cases presented in figures 3–5 are displayed in figure 6*a*(i–iii), respectively, for comparison with the steady flow pattern (figure 2*b*). All the time-averaged WSS patterns were at least broadly similar to the steady flow result, with low WSS at the sides and downstream of the orifice and elevated values around the ostial lip, upstream of it, and further downstream. The pattern for *non-reversing* side-branch flow (figure 6*a*(i)) was essentially identical to the steady flow result. For *reversing* side-branch flow (figure 6*a*(ii)), the high WSS region downstream of the branch was diminished and displaced further downstream; the downstream low WSS region became wider. Around the ostial lip, the high WSS region was enlarged by approximately $0.12D$ to the sides, $0.15D$ downstream and $0.03D$ upstream. Surface streamlines in the downstream area diverged less than those in the steady flow result. When the near-wall aortic flow *reversed* for part of the cycle (figure 6*a*(iii)), the high WSS region downstream of the ostium was extended and shifted upstream, slightly shrinking the downstream low WSS area. The region of high values around the ostium enlarged by approximately $0.17D$ in the upstream direction and $0.02D$ to the sides, and shrank by about $0.02D$ in the downstream direction. The streamline pattern was similar to the steady flow case, although streamlines diverged more in the downstream area.

3.6. Oscillatory shear index

Figure 6*b*(i–iii) shows maps of the OSI corresponding to the instantaneous WSS patterns of figures 3–5, and the time-averaged patterns of figure 6*a*(i–iii), respectively. For *non-reversing* flow in the aorta, regardless of whether the side-branch flow reversed or not (figure 6*b*(i)(ii)), the index had low values everywhere except in a circumscribed region downstream of the ostium, where it was elevated. This region took on a different shape for each case: a thin strip with three inner locations of highest OSI values (figure 6*b*(i)) or a semicircle of highest OSI values (figure 6*b*(ii)), and it was greater when the side-branch flow reversed for part of the cycle (figure 6*b*(ii)).

For flow involving *reversal* of the near-wall fluid in the aorta (figure 6*b*(iii)), the OSI had a pattern, which was almost the negative image of the time-averaged result (figure 6*a*(iii)), with low OSI values around the branch ostium, upstream and further downstream, and elevated OSI values laterally and slightly downstream. The result suggests that temporal oscillations of the WSS vector were greatest in regions lateral to the branch and coincided with low values of time-averaged WSS.

4. DISCUSSION

The present study is a continuation of our earlier work [4], in which Reynolds number and flow partition were found to have a substantial influence on the pattern of aortic WSS around an idealized aorto-intercostal branch ostium. It was motivated by observations of Sloop *et al.* [23], who measured flow waveforms by Doppler ultrasound in human subjects of different ages in an attempt to explain the change in pattern of aortic fatty streaks that occurs in early middle age. They detected late systolic/early diastolic retrograde flow in the thoracic aorta and intercostal arteries of healthy young men, but the phenomenon decreased and then disappeared with increasing age. The effects of these changes on WSS could not be estimated in their study.

We used steady flow in both vessels as a reference against which to compare the effects of pulsatility and

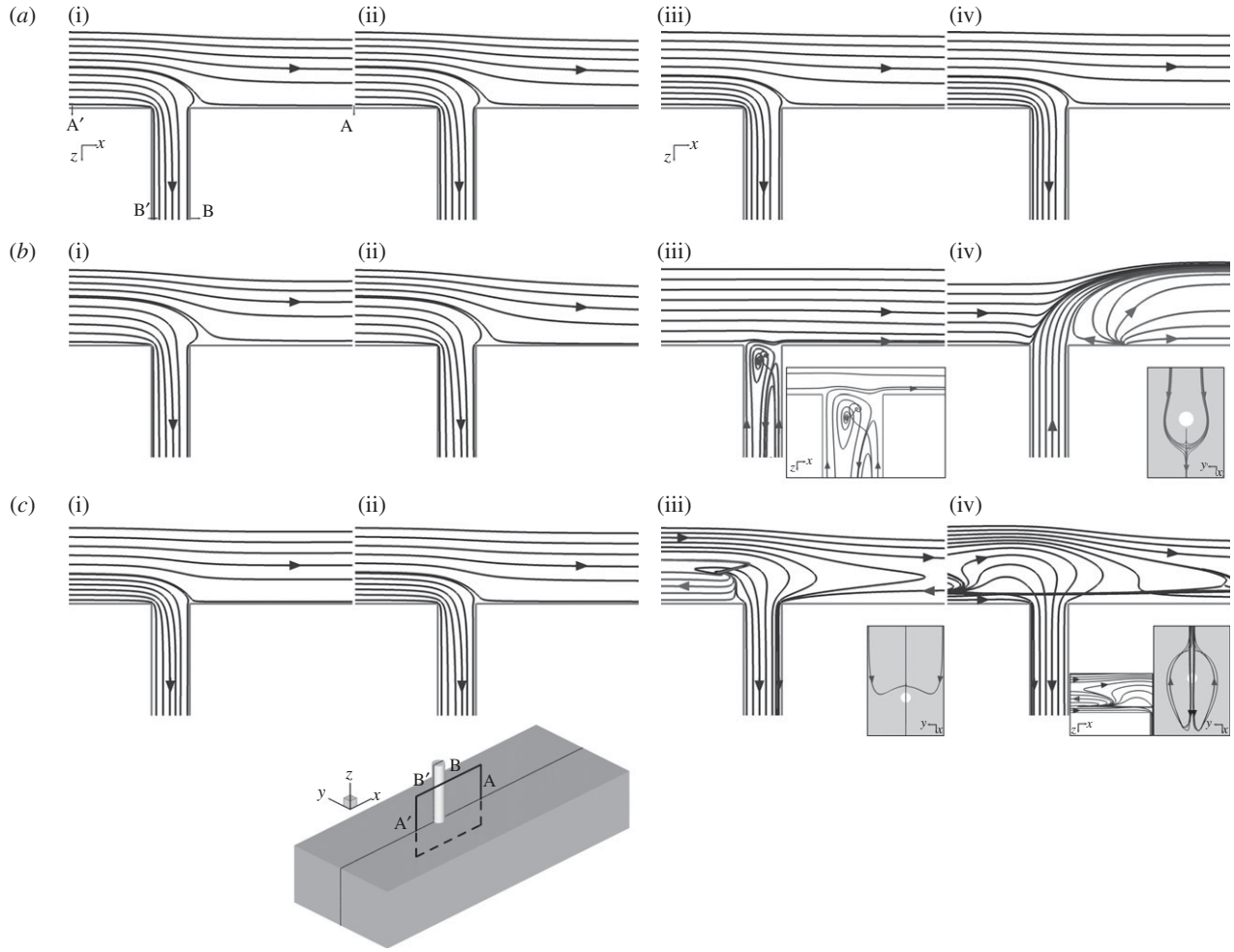

Figure 7. Instantaneous streamlines along the mid-plane of the aorto-intercostal junction for (*a*) non-reversing pulsatile side-branch flow and steady flow in the aorta, (*b*) reversing pulsatile side-branch flow and steady flow in the aorta, and (*c*) non-reversing pulsatile side-branch flow and reversing aortic near-wall flow. The cases correspond to the aortic WSS patterns displayed in figures 3–5, respectively ($Re_m = 500$, $Q_b : Q_{am} = 0.79\%$). Time points shown: $t/T =$ (i) 0.225, (ii) 0.475, (iii) 0.725 and (iv) 0.975 (Peak flow is at $t/T = 0.25$). Only a subregion of the computational domain is shown (length $6.8D \times$ height $5.15D$, on the mid-plane—see marked rectangle at the bottom right of figure 7 (i)(ii). Arrows indicate flow direction. Mean aortic flow is from left to right.

flow reversal. We examined pulsatile non-reversing and pulsatile reversing flow in the side branch, both with steady aortic flow. We also examined the effects of adding near-wall flow reversal in the aorta. (Effects of the branch do not propagate far towards the aortic centreline, so reversal of the bulk flow is immaterial.) To aid understanding of the fundamental flow physics, aortic flow reversal was combined with pulsatile non-reversing side-branch flow rather than the more complicated pulsatile reversing flow. When flow was pulsatile in the side branch and the aorta, the velocity waveforms were assumed to have the same frequency and to be in phase. Our main finding was that the instantaneous patterns of aortic WSS around intercostal ostia are greatly influenced by the existence of reversing side-branch flow (figure 4) or reversing aortic near-wall flow (figure 5) compared with steady flow (figure 2); pulsatile but non-reversing side-branch flow (figure 3), in contrast, had little effect.

To understand the mechanisms underlying these WSS patterns, instantaneous streamlines along the plane of symmetry of the aortic channel (i.e. the x–z plane through the centre of the branch) were computed for the four time points in the cycle for which instantaneous WSS patterns are presented in figures 3–5. For the case of pulsatile but non-reversing side-branch flow with steady aortic flow (figure 7*a*), the streamline that divides fluid entering the branch from that continuing down the aorta remained at almost the same distance from the wall (approx. $1.1D$) during the first half of the cycle (figure 7*a*(i)(ii)), but moved closer to the aortic wall towards the end of the deceleration phase (to approx. $0.85D$) and remained at that distance during the rest of the cycle (figure 7*a*(iii)(iv)). These variations were too small to change the aortic WSS substantially, as seen in figure 3.

For the case of *reversing* flow in the side branch (figure 7*b*), flow was anterograde in the side branch during the first half of the pulse (figure 7*b*(i)(ii)), and the lines were almost indistinguishable between these two time points. The dividing streamline was located approximately $1.3D$ above the aortic wall, an increase of $0.2D$ from the previous case. Changing the side-branch peak-to-mean flow ratio from 1.5 to 2.75 had

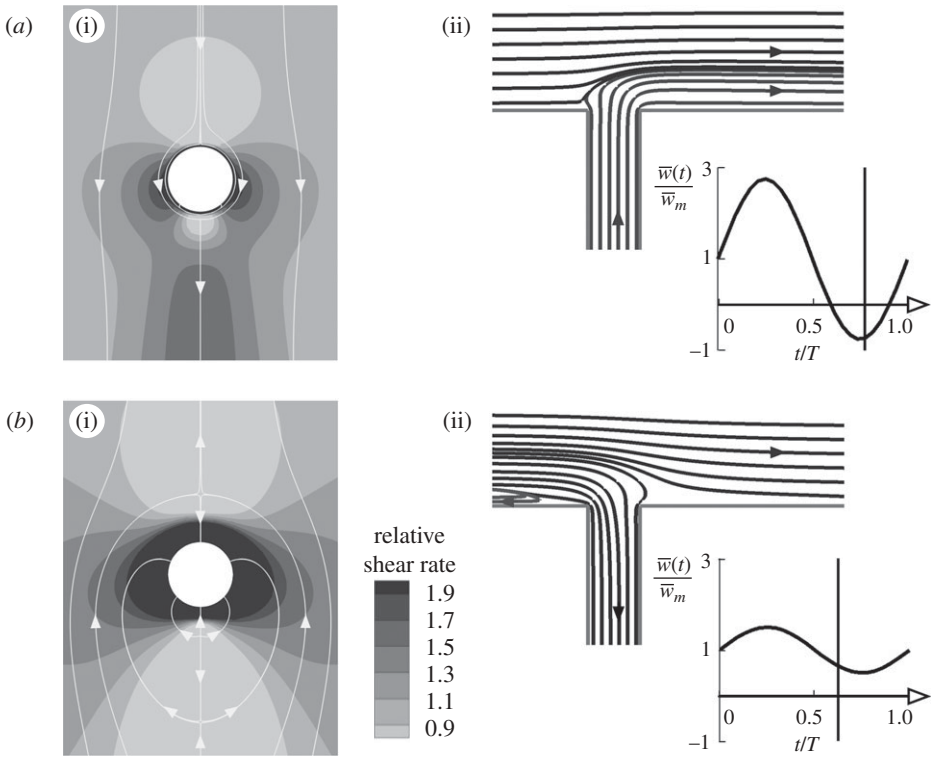

Figure 8. (i) Non-dimensionalized instantaneous aortic WSS and (ii) instantaneous streamlines along the mid-plane for (*a*) partially reversing flow at the side-branch (steady aortic flow, $Re = 500$, $t/T = 0.775$) and (*b*) partially reversing near-wall flow in the aorta (non-reversing pulsatile flow in the side branch, $Re_m = 500$, $t/T = 0.625$). Flow velocity in the side branch, averaged across its cross section and scaled by the time-averaged value, is plotted for each case in (ii).

this effect because more fluid needed to be drawn into the side branch. Increasing flow partition intensifies and enlarges features of WSS patterns, increasing particularly the high-shear regions upstream and around the ostium [4,24], as seen here in figure 4.

The onset of reverse flow occurred near the end of the deceleration phase of the cycle (figure 7*b*(iii)). Only a small jet of fluid, originally located near the rostral (anterior) wall of the intercostal artery, emerged from the side branch. Entering the aorta, it impeded the anterograde aortic flow upstream of the ostium, explaining the reduction in WSS in this region and the divergence of surface streamlines around it (figure 4*c*). The oncoming aortic flow forced the jet to move adjacent to the aortic wall immediately downstream of the branch, increasing WSS within a triangular region at that location. As flow within the side branch decreased to low levels, a vortex formed within its mouth, as depicted in the inset of figure 7*b*(iii). At the following time point (figure 7*b*(iv)), the jet of fluid from the branch protruded further into the aorta, causing the upstream aortic flow to change direction and move away from the wall. As a result, the upstream low-shear region enlarged and shifted further upstream while another low WSS region was formed downstream of the ostium (figure 4*d*). Surface streamlines in figure 4*d* suggest that aortic flow diverted around the ostium and converged at a distance approximately $1.5D$ downstream of it (shown also at the inset of figure 7*b*(iv) for lines slightly above the aortic wall). From that stagnation point, aortic fluid particles continued either further downstream in the aorta, or moved slightly upstream and away from the wall, occupying the space between the emerging jet of fluid and the aortic wall (figure 7*b*(iv)).

Figure 7*c* shows lines tangent to the instantaneous velocity vectors for pulsatile but non-reversing flow in the side branch, and pulsatile flow in the aorta that reverses near the wall. During the first half of the cycle (figure 7*c*(i)(ii)), the instantaneous dividing streamline was approximately $0.8D$ from the wall. This is closer than in figure 7*a*(i)(ii), consistent with the fact that flow in the aorta was pulsing in phase with the branch and the instantaneous flow partition near the peak flow was therefore smaller.

Near the end of the deceleration phase (figure 7*c*(iii)), the pattern of lines was profoundly altered. Fluid near the aortic wall flowed in the opposite direction to fluid further away from the wall, causing a small vortex at a location above and upstream of the branch mouth. Fluid particles from lateral locations upstream of the ostium also converged on the vortex (inset of figure 7*c*(iii)). Particles from the bulk aortic flow on the plane of symmetry were forced to enter the branch. Distal to the branch, reversing near-wall fluid also entered the branch.

Near the middle of the acceleration phase of the cycle (figure 7*c*(iv)), restoration of anterograde aortic flow started and the line pattern in the plane of symmetry became more complex. In the far upstream area, fluid particles up to $0.3D$ from the aortic wall entered the branch, fluid between $0.3D$ and $1D$ from the wall moved upstream (reverse flow), and fluid greater than $1D$ from the wall moved downstream and away from the wall, overshooting the ostium (figure 7*c*(iv), first inset). Some of the latter particles had complex paths,

reversing direction and occasionally entering the branch (second inset of figure 7*c*(iv)).

It is apparent that reverse flow has a strong influence on patterns of instantaneous aortic WSS around the ostium, but the time-averaged WSS patterns were not substantially affected; variations were observed mainly in the region downstream of the branch ostium. This apparent discrepancy (which is consistent with earlier results of Tuck [25] and DeMestre & Guiney [26]) may reflect the short lifetime of the features induced by reverse flow. This is demonstrated by figure 8, which displays instantaneous patterns for reverse flow in the side branch (figure 8*a*(i)) and reverse flow in the aortic near-wall region (figure 8*b*(i)), and their respective line patterns on the plane of symmetry (figure 8*a*(ii),*b*(ii)); the patterns in figure 8*a* were captured at $t/T = 0.775$ (i.e. closely following those already presented in figures 4*c* and 7*b*(iii) for $t/T = 0.725$) while those in figure 8*b* display patterns at the onset of reverse flow within the aorta, at $t/T = 0.625$ (preceding those shown in figures 5*c* and 7*c*(iii) for $t/T = 0.725$). It is apparent that large differences occur over these short intervals. For example, the vortex occurring as reverse flow initiates in the branch is quickly washed away as the cycle progresses.

The pattern of the OSI in the aorta was naturally least uniform when the aortic near-wall flow reversed for part of the cycle (figure 6*b*(iii)). (Interestingly, the pattern was similar in character to the one obtained by Buchanan *et al.* [27] for the much larger coeliac branch.) The condition that flow leaves the downstream end of the branch throughout the cycle required fluid to enter the branch. This occurred from regions downstream of and lateral to the ostium, in addition to regions further away from the wall. The deviation of the WSS vector from axial alignment was greater in the lateral regions than in the downstream and upstream regions. Temporal oscillations of the WSS vector (and hence OSI) were, therefore, greater lateral to the ostium than upstream and downstream of it (reduced OSI).

In our simulations and analyses, we made the simplifying assumptions of a Newtonian fluid and a flat, rigid and fixed aortic wall. Liepsch [28] has shown that non-Newtonian rheology has quantitative but not qualitative effects on WSS patterns near branches. We infer from studies by Secomb [29] and O'Dea & Waters [30] that for the flow regimes studied in this work and particularly for near-branch regions of the descending thoracic aorta, which are tethered to the posterior chest wall, the effects of wall-motion would be small. We also limited our investigation of pulsatile flow to a single mean Reynolds number and flow partition. Different steady WSS patterns occur for other pairs of values, as demonstrated by Kazakidi *et al.* [4]. However, new effects of reverse flow on WSS were demonstrated and some fundamental features of the flow underlying them were elucidated. A particularly interesting observation was the unexpected development of a vortex in the aorta, due to reversing aortic near-wall flow (figure 7*c*(iii)), and of another vortex in the side branch, owing to reversing side-branch flow (figure 7*b*(iii)). The high sensitivity of the instantaneous aortic WSS to these short-lived flow structures was surprising. Systems with moving walls, non-Newtonian rheology and other values of Re and $Q_b : Q_{am}$ are also expected to include such features.

This work was funded by the Institute of Biomedical Engineering, Imperial College London, the British Heart Foundation Center of Research Excellence, the Public Benefit Foundation Alexander S. Onassis and Fundación Caja Madrid. S.J.S. would also like to acknowledge partial support through an EPSRC Advanced Research Fellowship.

REFERENCES

1 Caro, C. G., Fitz-Gerald, J. M. & Schroter, R. 1971 Atheroma and arterial wall shear. Observation, correlation and proposal of a shear dependent mass transfer mechanism for atherogenesis. *Proc. R. Soc. Lond. B* **177**, 109–159. (doi:10.1098/rspb.1971.0019)

2 Ku, D. N., Giddens, D. P., Zarins, C. K. & Glagov, S. 1985 Pulsatile flow and atherosclerosis in the human carotid bifurcation. Positive correlation between plaque location and low oscillating shear stress. *Arteriosclerosis* **5**, 293–302.

3 Weinberg, P. D. 2002 Disease patterns at arterial branches and their relation to flow. *Biorheology* **39**, 533–537.

4 Kazakidi, A., Sherwin, S. J. & Weinberg, P. D. 2009 Effect of Reynolds number and flow division on patterns of haemodynamic wall shear stress near branch points in the descending thoracic aorta. *J. R. Soc. Interface* **6**, 539–548. (doi:10.1098/rsif.2008.0323)

5 Sherwin, S. J. & Karniadakis, G. E. 1996 Tetrahedral hp finite elements: algorithms and flow simulations. *J. Comput. Phys.* **124**, 14–45. (doi:10.1006/jcph.1996.0042)

6 Khan, S. & Haust, M. D. 1979 Variations in the aortic origin of intercostal arteries in man. *Anat. Rec.* **195**, 545–551. (doi:10.1002/ar.1091950313)

7 Caro, C. G., Pedley, T. J., Schroter, R. C. & Seed, W. A. 1978 *The mechanics of the circulation*. Oxford, UK: Oxford University Press.

8 Cornhill, J. F. & Roach, M. R. 1976 A quantitative study of the localization of atherosclerotic lesions in the rabbit aorta. *Atherosclerosis* **23**, 489–501. (doi:10.1016/0021-9150(76)90009-5)

9 Nichols, W. W. & O'Rourke, M. F. 1998 *McDonald's blood flow in arteries: theoretical, experimental and clinical principles*, 4th edn. London, UK: Arnold.

10 Pedley, T. J. 1980 *The fluid mechanics of large blood vessels*. Cambridge, UK: Cambridge University Press.

11 Sobey, I. J. 1977 Laminar boundary-layer flow past a two-dimensional slot. *J. Fluid Mech.* **83**, 33–47. (doi:10.1017/S0022112077001025)

12 Tutty, O. R. 1988 Flow in a tube with a small side branch. *J. Fluid Mech.* **191**, 79–109. (doi:10.1017/S0022112088001521)

13 Sherwin, S. J. & Blackburn, H. M. 2005 Three-dimensional instabilities and transition of steady and pulsatile axisymmetric stenotic flows. *J. Fluid Mech.* **533**, 297–327. (doi:10.1017/S0022112005004271)

14 Landau, L. D. & Lifshitz, E. M. 1959 *Fluid mechanics*. Oxford, UK: Pergamon Press.

15 Loudon, C. & Tordesillas, A. 1998 The use of the dimensionless Womersley number to characterize the unsteady nature of internal flow. *J. Theor. Biol.* **191**, 63–78. (doi:10.1006/jtbi.1997.0564)

16 Womersley, J. R. 1955 Method for the calculation of velocity, rate of flow and viscous drag in arteries when the pressure gradient is known. *J. Physiol.* **127**, 553–563.

17 He, X. & Ku, D. 1996 Pulsatile flow in the human left coronary artery bifurcation: average conditions. *J. Biomech. Eng.* **118**, 74–82. (doi:10.1115/1.2795948)
18 Peiró, J., Giordana, S., Griffith, C. & Sherwin, S. J. 2002 High-order algorithms for vascular flow modelling. *Int. J. Numer. Methods Fluids* **40**, 137–151. (doi:10.1002/fld.270)
19 Sherwin, S. J. & Peiró, J. 2002 Mesh generation in curvilinear domains using high-order elements. *Int. J. Numer. Methods Eng.* **53**, 207–223. (doi:10.1002/nme.397)
20 Giordana, S., Sherwin, S. J., Peiró, J., Doorly, D. J., Crane, J. S., Lee, K. E., Cheshire, N. J. & Caro, C. G. 2005 Local and global geometric influence on steady flow in distal anastomoses of peripheral by-pass grafts. *J. Biomech. Eng.* **127**, 1087–1098. (doi:10.1115/1.2073507)
21 Karniadakis, G. & Sherwin, S. J. 2005 *Spectral/hp element methods for computational fluid dynamics*, 2nd edn. Oxford, UK: Oxford Science Publications.
22 Sherwin, S. J., Shah, O., Doorly, D. J., Peiró, J., Papaharilaou, Y., Watkins, N., Caro, C. G. & Dumoulin, C. L. 2000 The influence of out-of-plane geometry on the flow within a distal end-to-side anastomosis. *J. Biomech. Eng.* **122**, 86–95. (doi:10.1115/1.429630)
23 Sloop, G., Perret, R., Brahney, J. & Oalmann, M. 1998 A description of two morphologic patterns of aortic fatty streaks, and a hypothesis of their pathogenesis. *Atherosclerosis* **141**, 153–160. (doi:10.1016/S0021-9150(98)00167-1)
24 Kazakidi, A. 2008 Computational studies of blood flow at arterial branches in relation to the localisation of atherosclerosis. PhD thesis, Imperial College London, London, UK.
25 Tuck, E. O. 1970 Unsteady flow of a viscous fluid from a source in a wall. *J. Fluid Mech.* **41**, 641–652. (doi:10.1017/S0022112070000800)
26 DeMestre, N. J. & Guiney, D. C. 1971 Low Reynolds number oscillatory flow through a hole in a wall. *J. Fluid Mech.* **47**, 657–666. (doi:10.1017/S0022112071001307)
27 Buchanan Jr, J. R., Kleinstreuer, C., Truskey, G. A. & Lei, M. 1999 Relation between non-uniform hemodynamics and sites of altered permeability and lesion growth at the rabbit aorto-coeliac junction. *Atherosclerosis* **143**, 27–40. (doi:10.1016/S0021-9150(98)00264-0)
28 Liepsch, D. W. 1990 Effect of blood flow parameters on flow patterns at arterial bifurcations—studies in models. In *Blood flow in large arteries: applications to atherogenesis and clinical medicine* (ed. D. W. Liepsch), pp. 63–76. Basel, Switzerland: Karger.
29 Secomb, T. W. 1978 Flow in a channel with pulsating walls. *J. Fluid Mech.* **88**, 273–288. (doi:10.1017/S0022112078002104)
30 O'Dea, R. D. & Waters, S. L. 2006 Flow and solute uptake in a twisting tube. *J. Fluid Mech.* **562**, 173–182. (doi:10.1017/S0022112006001194)